Decoherence and Revival in Attosecond Charge Migration Driven by Non-adiabatic Dynamics

Danylo T. Matselyukh[1], **Victor Despré**[2], **Nikolay V. Golubev**[3], **Alexander I. Kuleff**[2,*], **Hans Jakob Wörner**[1,*]

[1]Laboratorium für Physikalische Chemie, ETH Zürich, 8093 Zürich, Switzerland

[2]Theoretische Chemie, Physikalisch-Chemisches Institut (PCI), Universität Heidelberg, 69120 Heidelberg, Germany

[3]Laboratory of Theoretical Physical Chemistry, Institut des Sciences et Ingénierie Chimiques, EPF Lausanne, 1015 Lausanne, Switzerland

Abstract

Attosecond charge migration is a periodic evolution of the charge density at specific sites of a molecule on a time scale defined by the energy intervals between the electronic states involved. Here, we report the observation of charge migration in neutral silane (SiH_4) in 690 as, its decoherence within 15 fs, and its revival after 40-50 fs, using X-ray attosecond transient absorption spectroscopy. We observe the migration of charge as pairs of quantum beats with a characteristic spectral phase in the transient spectrum, in agreement with theory. The decay and revival of the degree of electronic coherence is found to be a result of both adiabatic and non-adiabatic dynamics in the populated Rydberg and valence states. The experimental results are supported by fully quantum-mechanical *ab-initio* calculations that include both electronic and nuclear dynamics, which additionally support the experimental evidence that conical intersections can mediate the transfer of electronic coherence from an initial superposition state to another one involving a different lower-lying state.

1 Introduction

Charge migration in molecules is a purely electronic process driven by a coherent superposition of electronic states, which can appear due to broadband excitation (1, 2) and/or electron correlation (3–5). The time scales of charge migration are therefore directly defined by the electronic states' energy separations (1, 6). Since the electronic states constituting a superposition state typically have differently shaped potential-energy

*Corresponding authors. alexander.kuleff@pci.uni-heidelberg.de, hwoerner@ethz.ch.

surfaces (PES), charge migration has been predicted to decohere rapidly because nuclear wavepackets evolving on different electronic states modulate the vertical energy interval or lose overlap in internal-coordinate or momentum space (7–10). Decoherence of charge migration can be expected to result in a fading of the periodic charge rearrangement, and thus, together with non-adiabatic population transfer, to a more permanent transfer of the charge (6,11), which can lead to bond-specific dissociation (12,13). As such, decoherence and non-adiabatic coupling are the key links between charge migration, that is by definition periodic in the few-states limit, and charge transfer, which is central to the further evolution of the induced dynamics and its final outcome (7–10).

The experimental observation of molecular charge migration remains a formidable challenge. Previous experiments have reported the reconstruction of attosecond charge migration in ionized iodoacetylene from high-harmonic spectroscopy (14) and the observation of ~4 fs quasi-periodic dynamics in the photofragmentation yield of ionized phenylalanine (15). These early results have triggered considerable theoretical activity (16–18), which has also studied the role of nuclear dynamics in charge migration (9, 19–22).

Here, we describe the observation of decoherence and revival of attosecond charge migration. We use the same carrier-envelope-phase-(CEP)-stable few-cycle laser pulse to separately excite charge migration in a neutral molecule, and generate a soft-X-ray (SXR) pulse that after a specified delay probes the dynamics through attosecond transient-absorption spectroscopy (ATAS, (23–25)). The choice of strong-field excitation was motivated by its high excitation fractions, as compared to single-photonexcitation. Whereas previous experiments on coherent superpositions of electronic states in neutral molecules have remained limited to the femtosecond time scale (26, 27) and charge-migration experiments have remained limited to molecular cations (14, 15), the present approach opens a pathway to studying charge migration in neutral molecules (28), while achieving sub-optical-cycle temporal resolution, thereby generalizing previous work on ground-state molecules (29) and doubly-excited states of helium (30). We find that the CEP-stable few-cycle pump pulse creates an electronic coherence between a valence- and a Rydberg-excited state, corresponding to a 690-as radial charge migration in SiH_4. Due to the differences in the associated PES, this electronic coherence is lost in ~15 fs as the vibrational wavepackets in different electronic states oscillate with different periods. The electronic coherence is found to revive after 40-50 fs, as the two nuclear wavepackets transiently recover position- and momentum-space overlap. Most interestingly, and supported by our theoretical analysis, the electronic coherence is found to partially transfer to a second pair of states, involving a dark valence and the same upper Rydberg-like state. Whereas the observed de- and recoherence of charge migration through electronically adiabatic vibrational dynamics have recently been predicted to occur in the iodoacetylene cation (10), we are not aware of a previous discussion of the transfer of electronic coherence, although it is related to the creation of electronic coherence at conical intersections (31, 32). Importantly, these results show that electronic coherence can not only revive after being suppressed due to nuclear motion, but can even be transferred to other electronic states through conical intersections.

2   Results and Discussion

2.1   Experimental Methodology and Results

Figure 1 presents the experimental scheme and ATAS results. A 5.2-fs CEP-stable laser pulse centered at 780 nm is used to excite silane (SiH_4) molecules in the gas phase. The induced dynamics are probed by the transient absorption of an isolated attosecond pulse (with an estimated sub-200-as duration) covering the silicon $L_{2,3}$-edge, as shown in Extended Data Fig. 1. The time delay between the two pulses is stabilized to <25 as using a dual laser- and white-light interferometer (33). Details on the experimental methods are given in the methods section and the supplementary material (SM, Section S1). Figure 1B illustrates the excitation/probing scheme. The few-cycle pulse simultaneously excites (I.a) and ionizes (I.b) the sample. These two pathways are observed in different spectral regions, as illustrated in Fig. 1C. SiH_4^+ is unstable in its electronic ground state and therefore dissociates to form $SiH_3^+ + H$. This fragmentation process occurs within 25 fs (34), manifesting as the appearance of a new absorption feature centred at 108 eV which then moves to higher energy to form two absorption bands between 108.7 eV and 109.4 eV, corresponding to SiH_3^+. This spectral assignment is confirmed by calculations that will be published elsewhere. These bands are also found to oscillate with a period of ~20 fs that matches the 40 fs out-of-plane umbrella vibration of SiH_3^+.

Henceforth, we concentrate on pathway I.a, i.e. strong-field excitation of superpositions of valence and Rydberg states of the molecule that lead to modulations of the absorption spectrum between 102 and 107.5 eV. Our assignment of the static X-ray absorption spectrum of silane is based on core-valence-separated extended algebraic-diagrammatic construction through second order (CVS- ADC(2)-x) calculations shown as sticks in the top panel of Fig. 2A. The broad absorption band at 102-104 eV can be fit with four Gaussian functions, corresponding to the spin-orbit-split excitations to $3t_2$ and $4a_1$ valence orbitals. The progression starting at 105 eV consists of $d(e/t_2)$- and s-Rydberg series. In addition to pure electronic transitions, the origins of which we have labeled, the absorption spectrum of silane is known to exhibit weaker vibronic peaks (not labeled or included in our stick spectra). All of our assignments agree with previous work (35), except for the relative ordering of the 3d(e) and 5s Rydberg states.

The most remarkable observation in Fig. 1C is the clear oscillation of the optical density (OD) in the spectral regions of 102-104 eV and 105.5-107.5 eV with a period of 1.31-1.39 fs that is observed to survive from delays where pump and probe pulses overlap (yellow shading) out to about 15 fs (lower dashed box and inset), and to transiently revive between 40 and 50 fs (upper dashed box and inset). These rapid oscillations are quantum beats and a signature of charge migration (36), resulting from the interference of pairs of quantum paths that share a set of common final states, as illustrated in Fig. 2B.

2.2   Identification of Quantum Beats

In ATAS, electronic coherences between two states with allowed transitions into a common final state are expected to appear as pairs of absorption peaks oscillating in intensity as a

function of delay (quantum beats), fulfilling the relation $E = h/T = h\nu$, where E is the energy separation of the electronic states (and therefore the photon energy separation of the absorption peaks), T the period and ν the frequency of the quantum beat.

To determine if our high frequency signals are indeed a signature of electronic coherence, they are spectrally analyzed in the central panel of Fig. 2A, which presents a fast Fourier transform (FFT) along the delay axis (for $t > 10$ fs) of the ATAS results in Fig. 1C (for details, see Section S1.3). The Fourier spectrum exhibits two distinct frequencies with large amplitudes - 0.720 PHz (2.98 eV) and 0.765 PHz (3.16 eV). In the X-ray spectrum, both Fourier frequencies appear as two similar sets of peaks (102.5-104.5 eV and 105.5-107.5 eV) separated by ~3 eV, in agreement with the the quantum beat frequency.

The consistency between spectral and Fourier signals is even better than at first glance. Owing to their photon energy overlap, the Fourier peaks in the Rydberg region are used as references (vertical white-to-grey shaded lines in Fig. 2A) and, tracing the corresponding diagonal lines according to $\nu = E/h$, all strong FFT signals are paired up. The line-out of the FFT amplitude at 0.72 PHz (bottom panel of Fig. 2A) demonstrates this more clearly by shifting a copy of the spectrum by the corresponding 2.98 eV. With the additional investigation of the phase of the quantum beats, discussed in section 2.5, we are able to definitively assign these fast oscillations of the OD to quantum beats between pairs of coherently populated electronic states, corresponding in space to molecular chargemigration, and not to other possible light-induced artifacts. The time-evolution of these signals can therefore be taken to represent the time-resolved coherence and further investigated to determine the effect nuclear dynamics have on electronic coherences.

Furthermore, the spectral position of the FFT signals with respect to the ground-state absorption spectrum of silane (top of Fig. 2A) can also reveal the electronic configurations of the pump-prepared electronic states. The spectral overlap of 105-107 eV Fourier signals with the ground state Rydberg absorption lines (being blue-shifted by only 60 meV) indicates that the higher-lying state of both the 0.72-PHz and the 0.765-PHz coherence can only consist of an excitation into the $5a_1$ orbital of 5s-Rydberg character. The observed spectral alignment is the consequence of the insensitivity of core-Rydberg transition energies to the valence electronic excitation. Such an insensitivity has also been found in the case of IBr, where valence excitation caused a shift of less than 0.5 eV of 4d-core-Rydberg transitions (25). The shift of the lower-lying and more spatially confined 2p-orbitals should be even smaller. By contrast, any states with 3d(e)-Rydberg character would instead produce signals around 105.0 eV, which are not observed. The lower-lying states involved in the two coherences lie in the 102-104 eV spectral region, which uniquely identifies them as valence-excited states. The $2t_2 \rightarrow 3t_2$ and $2t_2 \rightarrow 4a_1$ excitations are the only possible assignments, leading to the configurations given in Fig. 2B.

To relate these electronic configurations to specific valence-excited states, we performed equations-of-motion coupled-cluster singles-doubles (EOM-CCSD) calculations using an augmented correlation-consistent valence-triple-zeta (aug-cc-pVTZ) basis set (see SM, Section S2.1). The calculated electronic spectrum is compared to the measured valence-absorption spectrum of silane in Fig. 2C. The $(2t_2^{-1} 5a_1^1)$ and $(2t_2^{-1} 4a_1^1)$ configurations each

give rise to a single state, with T_2 symmetry, henceforth designated as C and B states, respectively. The $(2t_2^{-1}3t_2^1)$ configuration gives rise to a total of four electronic states of symmetries T_1, E, A_1 and T_2. Among those, the T_1 state is the only one to lie below the B state (see Fig. S4), matching the ~3 eV energy spacing observed in the experiment. Owing to its T_1 symmetry, this state labelled A, is dark in the single-photon absorption spectrum. The contribution of the A, B and all other valence states to the observed quantum beats is determined with the help of fully quantum simulations.

2.3 Fully Quantum Simulations of Electronic and Nuclear Dynamics

Multiconfigurational time-dependent Hartree (MCTDH) calculations (37, 38) were performed on a manifold of 15 excited electronic states, including all four vibrational stretching modes of silane. PES of the lowest 16 states were calculated (Fig. 3A) at the EOM-CCSD/aug-cc-pVTZ level. These PES were then used to fit the parameters of a second-order vibronic-coupling Hamiltonian (39) that includes both non-adiabatic and Jahn-Teller interactions. These calculations provide a fully quantum-mechanical description of electronic and nuclear dynamics. Details of these calculations are discussed in the SM, section S2.2.

The strong-field nature of the pump pulse coupled to remaining experimental instabilities can be expected to influence the detailed initial superposition state in which the system is prepared, which deserves a careful discussion. The effect of the initial phase on the dynamics is considered by running multiple MCTDH simulations with randomised phases (for details see Section S2.3), the result of which is represented by the shaded areas in Fig. 3B and 4B. The less restrictive selection rules of multiphoton excitation compared to single-photon excitation were accounted for by studying two limiting cases. In the first case, all states contained in the MCTDH model were populated and in the second case, only the dipole allowed B and C states were initially populated. In both limiting cases the population in the C state remained con stant over time. In the first case, the populations of the intermediate states were found to relax to the B and A states within 10 fs (Fig. S7). In addition to the BC and AC coherences, these calculations predicted additional coherences at 0.65 PHz and 0.58 PHz (see Fig. S7), which are weak and not observed, respectively, in the FFT shown in Fig. 2A. In the second limiting case, the population initially prepared in the B state was found to partially relax to the A state in ~7 fs (Fig. 3B). This B-A population transfer is mediated by conical intersections along the ν_4 vibrational mode, shown in Fig. 3A (right) and visible in the dynamics of Movie S2. In agreement with the experiment (Fig. 2A), these calculations exclusively predict the appearance of BC and AC coherences. This comparison supports the predominant long-lived coherent excitation of the B and C states by the pump pulse, although the excitation of the other valence states is not ruled out. The apparent spectral selectivity is consistent with few-cycle excitation in the strong-field regime, which results in spectral excitation windows (as further explained in SM Section S2.6), in analogy with strong-field ionization (40).

We therefore from hereon focus on the simplest model that reproduces the experimental observations – the initial population of the B and C states only. The calculated electronic coherences are shown in Fig. 4B. The BC coherence appears at $t = 0$, whereas the AC

coherence progressively builds up, reaching a maximum around 7 fs. These results show that the electronic coherence between the B and C states is efficiently transferred to a coherence between the A and C states, mediated by the non-adiabatic population transfer from B to A. Experimental evidence in support of such a transfer is shown in Extended Data Fig. 2 and discussed further in Section S1.2.2.

2.4   Attosecond Charge Migration and its Revival

We now turn to the detailed analysis of the attosecond charge migration and its evolution on the femtosecond time scale. Here we have chosen to compare the quantum beat measured at a particular photon energy with the MCTDH results directly, such that the assumptions necessary for reconstructing a full transient spectrum using equation S7, as detailed in section S2.3, do not have to be made. Figure 4B shows the 0.5 to 1.5 PHz components of the   OD signal averaged over the 105.51-105.66 eV energy window. The signal displays the 1.31-1.39 fs period quantum beats that have been identified in Fig. 2. The initial decoherence of the quantum beat and the revival between 40 and 55 fs are also evident. A direct comparison between the amplitudes of the experimental signal oscillation and the calculated electronic BC and AC coherences shows excellent agreement up to a small offset in the timing of the maximal revival.

The right-hand side of Fig. 4 elucidates the origin of this decay and revival of the BC coherence. Whereas it is clear that nuclear dynamics are responsible for the modulation of the coherence, the time scale of 50 fs is far longer than any vibrational periods included in the MCTDH model. As can be seen in Fig. 4C, which shows the autocorrelation of the nuclear wavepackets in the different electronic states (R_{ii}), these complete multiple periods of vibration before the peak of the coherence revival. Whereas the dynamics on the C state are adiabatic and periodic, the wavepacket prepared on the B state exhibits non-adiabatic population transfer and therefore an autocorrelation function that does not return to its initial value.

For coherence between two electronic states i and j to be observed in an experiment, they must both hold significant populations (p_i, p_j) and their vibrational wavepackets must have a non-zero overlap not only in coordinate space ($O_{ij} = e^{-\Delta Q_{ij}^2}$, where Q_{ij} is the spatial separation), but also in momentum space ($D_{ij} = e^{-\Delta P_{ij}^2}$, where P_{ij} is the momentum separation). To eliminate the (trivial) effect of the population dynamics, we follow Refs. (41, 42) and define the normalised electronic coherence, which is given by the product between O_{ij} and D_{ij}. Since these quantities are not directly accessible in the calculations, they were obtained within a Gaussian approximation to the vibrational wavepackets (43); the corresponding quantities are shown in panels D and E (for details see SM, Section S2.4). As expected, the product of O_{ij} and D_{ij} evolves similarly to the normalised magnitude of the BC coherence ($|\chi_{BC}|/\sqrt{p_B p_C}$) from the MCTDH calculation (panel F). Movie S2 shows that the source of this effect is mainly the ν_3 mode, which, unlike the ν_4 mode, exhibits a strong displacement between the equilibrium geometries of the ground and excited states, resulting in large-amplitude motion and significant separation of the respective vibrational wavepackets. Our calculations thus show that, due to the relative curvature of the ν_3

PES of the B and C states, it takes approximately 50 fs for the nuclear wavepackets to simultaneously regain coordinate- and momentum-space overlap, producing the revival.

To tie this analysis into the general topic of electronic decoherence in molecules, we can apply the terminology of (22) (which itself applies the semiclassical theory of decoherence proposed in (44) to molecular systems). The first contribution, the "change in the electronic state populations", is shown in Fig. 3 and has been factored out in Fig. 4. The second, the "decrease of the overlap between the nuclear wave packets on different electronic states", is captured by the product of O_{ij} and D_{ij}, shown in green in Fig. 4F. The remaining difference between the product and the population-normalised coherence (shown in purple) can be attributed to the third decoherence contribution, i.e. the "dephasing of the different wave packet components".

Having identified the experimentally observed coherences, we can combine all results to reconstruct the electronic density as a function of time. The spatial structure of the charge migration is defined by the transition densities ($\langle \psi_i | \hat{\rho} | \psi_j \rangle$, where $\hat{\rho}$ is the EOM-CC density operator). The two most relevant ones are shown on the right-hand side of Fig. 4A. Whereas the BC coherence causes charge to travel along the Si-H bond direction, the AC coherence causes it to migrate between pairs of hydrogen atoms.

The time-dependent difference electron density with respect to the SiH_4 ground state resulting from applying the MCTDH coherences to these transition densities is shown in Fig. 4A. $t_{CM} = 0$ has been chosen to correspond to times when the electron density is most strongly contracted around the molecule, resulting in an increase of core-Rydberg hole overlap and therefore the experimentally observed OD at 105.5 eV. The complete temporal evolution of charge migration is shown in a supplementary movie (Movie S1). The differently shaped transition densities can give rise to interesting phenomena - depending on the relative amplitude of the coherences ($|\chi_{ij}|$), the charge migration can change from being radial to angular in nature, particularly noticeable at 40 and 60 fs in Movie S1.

2.5 Phase of Quantum Beats

Finally, we turn to the phase of the observed electronic quantum beats and analyze their information content. Figure 5A shows the simulated transient spectrum and associated FFT phase of the simplest possible system that can produce a quantum beat in ATAS – a coherent 3-level system. The analyticalform of the signal can be found in section S2.3 equation S7 and corresponds very well to previous experimental work on atoms (23). Although the phase of the quantum beat of the two lines is equal at the peak of the   OD amplitude, the phase to the sides of these maxima are mirrored, producing a characteristic 'U'-shaped phase profile. Such a signal is clearly distinct from few-femtosecond oscillations found in more common XUV-pump–IR-probe ATAS measurements, where the phase is initially flat and steepens towards larger negative delays (this is most evident when a Gabor filter is applied to the data, which is further analysed in section S1.2 and visible in Fig. S2).

Figure 5C shows the phase of the FFT of the BC coherence. In agreement with the simulated 3-level system each quantum beat pair also displays mirrored phase profiles, experimentally identifying them as quantum beats. The much larger total variation of the

phase in Fig. 5C compared to 5A is a result of the summation of the phase steps of spectrally adjacent core-valence transitions. The total phase variation therefore contains information both on the number of final core-excited states and on the relative phases of their transition-dipole moments, also known as the transition-dipole phase (TDP), a property of growing importance in attoscience (45, 46). The signature of the TDP on the quantum beats also carries an important physical meaning (which, up to now, has not been accessible due to the limited number of final states in previously studied atomic systems): out-ofphase quantum beats are the experimental manifestation of the charge migration (46). When electronhole density migrates, its overlap with the different Rydberg orbitals changes, periodically modulating the probability of different core-valence excitations. The experimental observation of these out-ofphase signals is thus a direct measure of charge migration.

To demonstrate the sensitivity to the TDP, ATAS simulations (36) have been performed based on the MCTDH dynamics the results of which are shown in Fig. 5B, which compares two simulations (see section S2.3 for details). To simplify the analysis, we neglected the vibrational structure of the final core-excited electronic states, thus concentrating on the electric dipole transitions between the initial and final electronic states. The simulated transient spectra use the same absolute transition dipole values and transition energies for the A, B, and C to final core-excited-state transitions, however, in the upper panel the signs of the transitions from the C state to the final states have been chosen to alternate as a function of energy (see Table S4), whereas equal signs have been used in the lower panel. Clearly, the sign alternation is required to reproduce the monotonic phase variation observed in the experiment. Moreover, the total phase variation is a signature of the number of final states. In our simulations, we have assumed 3 final states to be accessible from A, 7 from B, and all ten of them from C. This model calculation results in reasonable agreement with the experimental data, whereby the smaller calculated phase variation suggests that the number of final states is even larger in reality. This is not unexpected, because of the doubly-excited (core+valence) character of the final states, but the quantitative description of these states is beyond the capabilities of state-of-the-art quantum-chemical calculations. Nevertheless, this analysis demonstrates the sensitivity of ATAS to the TDP, an observable that is not accessible in conventional spectroscopy.

3   Conclusion

This work has uncovered some remarkable opportunities in molecular attosecond spectroscopy. ATAS is capable of capturing specific electronic coherences in spite of the nearly featureless valence absorption spectrum (Fig. 2C). This is a direct consequence of the high temporal resolution on one hand, and the selectivity of the SXR-ATAS observables on the other. On the observed time scales, structural dynamics are limited to a subset of high-frequency stretching modes, which enables the preparation and survival of a complex electronic wavepacket that shows decoherence and revival. This information can not be obtained from the frequency-domain spectra, which are complicated by large-amplitude motions, driven by the Jahn-Teller effect that take place on longer time scales and involve the bending modes. On the investigated time scales, the quantum system can be thought of as evolving under the action of a simplified Hamiltonian that only contains

the electronic and high-frequency vibrational modes, resulting in qualitatively simpler dynamics. The specificity of the SXR-ATAS observablesarises from the projection of the dynamics under scrutiny onto common sets of Rydberg-like core-excited states. Since this probe step involves core excitations from and into orbitals with weak electron correlation, they should be analogous to those of the unexcited molecule; a similarity which is key to the straightforward assignment of the dynamics. The present method can thus be expected to favorably scale towards more complex molecules, since both the time-scale and the spectral-simplification arguments are general.

Our results moreover show the possibility of preparing and observing charge migration in neutral molecules, while achieving a temporal resolution that lies significantly below the duration of the pump pulse. Specifically, we have observed the decoherence and revival of attosecond charge migration driven by structural and non-adiabatic dynamics. These results show that charge migration can not only survive coupled electron-nuclear dynamics, characteristic of excited-state dynamics in large molecules, but even be transferred to other electronic states. These observations also confirm the viability of the proposed control schemes over electronic degrees of freedom for manipulating chemical dynamics (47). An immediate extension of our results is the control over attosecond charge migration (48), its application to steer charge transfer to a desired outcome and to thereby control chemical reactivity. All of these pillars of attosecond chemistry have now come within reach of experimental capabilities.

Methods

Presentation of errors

The error bars of the theoretical results represent the standard deviation per time step of all phase- randomised simulations when coherently averaged. For experimental result, due to the SVD filtering, the standard deviation over multiple measurements in not indicative of the true accuracy of the instrument. Instead, the error is estimated by taking the standard deviation of the OD with respect to delay in a spectral region exhibiting no time-resolved signal (<91 eV) and evaluated as 2.9 mOD.

Experimental setup

An amplified carrier-envelope-phase (CEP) stabilized titanium:sapphire laser system (FEMTOPOWER V CEP) was used to deliver 25 fs, 1.5 mJ near-infrared (NIR) pulses centered at 790 nm with a full width at half maximum (FWHM) of 70 nm. These pulses were spectrally broadened in a 1 m-long, helium-filled hollow-core fibre. The gas pressure was adjusted such that the transmission efficiency of the fiber did not drop when helium gas was introduced, producing a spectrum spanning >350 nm with a central wavelength of 780 nm. Due to the third-order spectral phase imprinted onto the pulse by the broadening process (50), the pulse is compressible to 5.2 fs using broadband chirped mirrors and glass wedges (measured using a home-built, second-harmonic d-scan device).

Once compressed, the >500 μJ pulse was used to drive high-harmonic generation in a finite gas target filled with helium. A parabolic collimating mirror with a hole was used to

separate thetransmitted fundamental beam from its high harmonics, reflecting the diverging driving field while allowing the high-harmonic attosecond pulses to pass through. A 200 nm-thin zirconium foil was used to isolate the soft-X-ray pulse from the weak residual driving field before recombination. To avoid damaging the gold-coated toroidal refocusing mirror with the shorter-wavelength portion of the driving field, the filtering was performed directly in front of the toroid. In addition, two Nb_2O_5-coated mirrors were employed as partial beamsplitters to lower the driving field intensity, preventing the Zr filter from melting. A second parabolic mirror with a center hole placed after the toroidal allowed the attosecond high-harmonic pulse to pass through, collinearly recombining it with the recycled driving field while focusing the latter. The delay between the pump and the probe pulse is actively stabilised with a He-Ne interferometer and additionally monitored with white-light interferometry resulting in a delay jitter of <25 as. Additional details on the basic experimental setup are given in (33).

The two pulses were focused into a 1 cm-long gas cell which was filled with the target gas. The spatial overlap between the pulses was optimized by maximizing the absorption signal from strong-field-ionized krypton. Time-zero was defined using the onset of the Kr^+ $M_{4,5}$-edge absorption signal. By recycling the driving pulse after high-harmonic generation, any additional nonlinear process that occurs inside the HHG target affects not only the generated harmonics but also the NIR pump pulse, which contributes to achieving an optimal temporal stability between the strong-field pump and the soft-X-ray (SXR) probe pulse.

The transmitted spectrum was recorded using a CCD-based soft-X-ray spectrometer with sub-100 meV resolution at 100 eV, achieved by using a backlit in-vacuum CCD camera with a flat-field grating. The background signal from the residual driving field was minimized by using another 200-nm-thin Zr filter preceded by a pinhole which spatially removed a large portion of driving field, thus protecting the metallic filter from damage.

Data acquisition and processing

The active interferometric stabilization of our beamline allows the delay to be set to a specific value repeatedly. As such, each ATAS measurement performed on our beamline can include multiple scans of the same delay time resulting in a higher sensitivity. For the measurement presented in this work, two scans were preformed over a delay range of −20 fs to 70 fs with a step size of 250 as. For each scan and delay, exposures of 2 seconds were taken with the pump arm blocked and then unblocked. Before the measurement was started, a set of reference measurements were performed to establish the source of the different background signals and to allow for their subtraction. First, both the pump and probe arms were blocked and the dark counts of the CCD camera were captured. This exposure was used as a background for frames with the NIR arm blocked. Next, the probe arm was unblocked, providing a reference SXR spectrum to allow for the absolute absorption to be computed. Finally, since the pump pulse is sufficiently short and intense to produce harmonics in the target gas, only the pump arm was unblocked and the target filled with gas to provide a background for measurements with the pump arm unblocked.

To maximize the resolution of our spectrometer, as required to resolve the fine structure of the silane $L_{2,3}$ absorption spectrum, the curved nature of the spectral images produced by

the flat field grating needs to be compensated for (51). This is done by taking an average of the reference measurements over all delays and analyzing each row of the resulting reference image individually. For each row, the centre of mass of different absorption features is calculated. A cubic fit is performed to determine the position of the absorption features as a function of the vertical position on the CCD. This function is then used to shift the rows with respect to each other such that the absorption features line up with each other, allowing for a corrected, higher resolution spectral flux to be calculated. The horizontal pixel axis is converted into the photon energy axis by adjusting parameters in the grating equation until optimum overlap is achieved with the literature absorption spectrum of silane (35), resulting in Extended Data Figure 1 (and Fig. 1C in the main text).

Extended Data
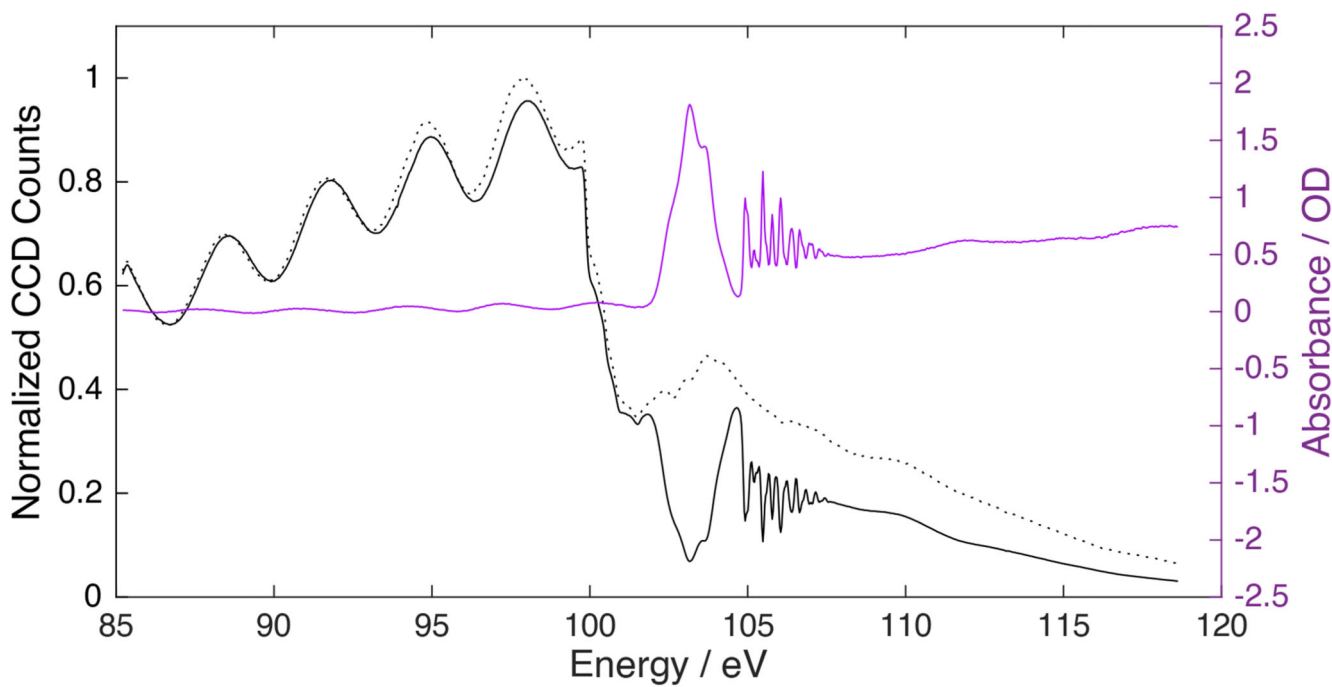
Extended Data Fig. 1.
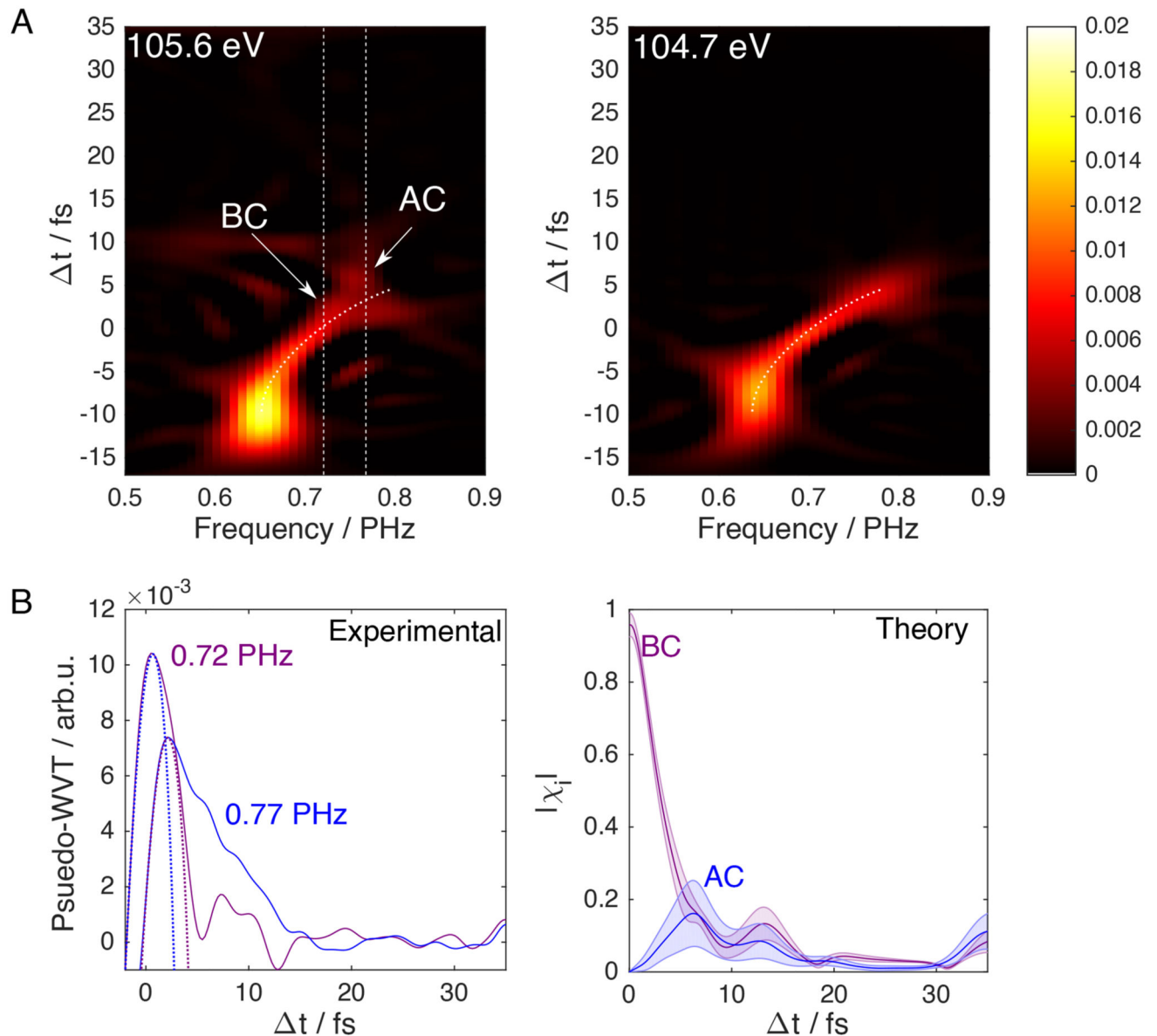
Extended Data Fig. 2.

Supplementary Material

Refer to Web version on PubMed Central for supplementary material.

Acknowledgments

Data Availability Statement

Source data are available for this paper. All other data that support the plots within this paper and other findings of this study are available from the corresponding author upon reasonable request.

References and Notes

1. Eyring, H, Walter, J, Kimball, GE. Quantum chemistry. Wiley; 1944.

2. Remacle F, Levine RD. An electronic time scale in chemistry. PNAS. 2006; 103: 6793–6798. [PubMed: 16636279]

3. Cederbaum LS, Zobeley J. Ultrafast charge migration by electron correlation. Chemical Physics Letters. 1999; 307: 205–210.

4. Kuleff AI, Cederbaum LS. Ultrafast correlation-driven electron dynamics. Journal of Physics B: Atomic, Molecular and Optical Physics. 2014; 47 124002 doi: 10.1088/0953-4075/47/12/124002

5. Kraus PM, Wörner HJ. Perspectives of attosecond spectroscopy for the understanding of fundamental electron correlations. Angew Chem Int Ed. 2018; 57: 2–22.

6. Wörner HJ, et al. Charge migration and charge transfer in molecular systems. Structural dynamics. 2017; 4 061508 [PubMed: 29333473]

7. Vacher M, Steinberg L, Jenkins AJ, Bearpark MJ, Robb MA. Electron dynamics following photoionization: Decoherence due to the nuclear-wave-packet width. Phys Rev A. 2015; 92 040502 doi: 10.1103/PhysRevA.92.040502

8. Arnold C, Vendrell O, Santra R. Electronic decoherence following photoionization: Full quantum-dynamical treatment of the influence of nuclear motion. Physical Review A. 2017; 95 033425

9. Despré V, Golubev NV, Kuleff AI. Charge migration in propiolic acid: A full quantum dynamical study. Physical Review Letters. 2018; 121 203002 [PubMed: 30500257]

10. Jia D, Manz J, Yang Y. De-and recoherence of charge migration in ionized iodoacetylene. The Journal of Physical Chemistry Letters. 2019; 10: 4273–4277. [PubMed: 31287313]

11. Lünnemann S, Kuleff AI, Cederbaum LS. Ultrafast charge migration in 2-phenylethyl-n, n-dimethylamine. Chemical Physics Letters. 2008; 450: 232–235.

12. Remacle F, Levine R, Ratner MA. Charge directed reactivity: a simple electronic model, exhibiting site selectivity, for the dissociation of ions. Chemical physics letters. 1998; 285: 25–33.

13. Lehr L, Horneff T, Weinkauf R, Schlag E. Femtosecond dynamics after ionization: 2-phenylethyl-n, n-dimethylamine as a model system for nonresonant downhill charge transfer in peptides. The Journal of Physical Chemistry A. 2005; 109: 8074–8080. [PubMed: 16834192]

14. Kraus PM, et al. Measurement and laser control of attosecond charge migration in ionized iodoacetylene. Science. 2015; 350: 790–795. [PubMed: 26494175]

15. Calegari F, et al. Ultrafast electron dynamics in phenylalanine initiated by attosecond pulses. Science. 2014; 346: 336–339. [PubMed: 25324385]

16. Despré V, et al. Attosecond hole migration in benzene molecules surviving nuclear motion. The Journal of Physical Chemistry Letters. 2015; 6: 426–431. DOI: 10.1021/jz502493j [PubMed: 26261959]

17. Yuan K-J, Bandrauk AD. Exploring coherent electron excitation and migration dynamics by electron diffraction with ultrashort x-ray pulses. Phys Chem Chem Phys. 2017; 19: 25846–25852. DOI: 10.1039/C7CP05067D [PubMed: 28932829]

18. Jia D, et al. Quantum control of electronic fluxes during adiabatic attosecond charge migration in degenerate superposition states of benzene. Chemical Physics. 2017; 482: 146–159.

19. Vacher M, Meisner J, Mendive-Tapia D, Bearpark MJ, Robb MA. Electronic control of initial nuclear dynamics adjacent to a conical intersection. J Phys Chem A. 2014; 119: 5165–5172. [PubMed: 25466408]

20. Lara-Astiaso M, Palacios A, Decleva P, Tavernelli I, Martín F. Role of electron-nuclear coupled dynamics on charge migration induced by attosecond pulses in glycine. Chemical Physics Letters. 2017; 683: 357–364.

21. Sun S, et al. Nuclear motion driven ultrafast photodissociative charge transfer of the penna cation: An experimental and computational study. The Journal of Physical Chemistry A. 2017; 121: 1442–1447. DOI: 10.1021/acs.jpca.6b12310 [PubMed: 28135094]

22. Vacher M, Bearpark MJ, Robb MA, Malhado JaP. Electron dynamics upon ionization of polyatomic molecules: Coupling to quantum nuclear motion and decoherence. Phys Rev Lett. 2017; 118 083001 doi: 10.1103/PhysRevLett.118.083001 [PubMed: 28282194]

23. Goulielmakis E, et al. Real-time observation of valence electron motion. Nature. 2010; 466: 739–743. DOI: 10.1038/nature09212.1203.3119 [PubMed: 20686571]

24. Timmers H, et al. Disentangling conical intersection and coherent molecular dynamics in methyl bromide with attosecond transient absorption spectroscopy. Nature Communications. 2019; 10: 1–8.

25. Kobayashi Y, Chang KF, Zeng T, Neumark DM, Leone SR. Direct mapping of curvecrossing dynamics in ibr by attosecond transient absorption spectroscopy. Science. 2019; 365: 79–83. [PubMed: 31273121]

26. Kraus PM, et al. High-harmonic probing of electronic coherence in dynamically aligned molecules. Phys Rev Lett. 2013; 111 243005 doi: 10.1103/PhysRevLett.111.243005 [PubMed: 24483654]

27. Walt SG, et al. Dynamics of valence-shell electrons and nuclei probed by strong-field holography and rescattering. Nat Comm. 2017; 8 15651 doi: 10.1038/ncomms15651

28. Dutoi AD, Cederbaum LS. An excited electron avoiding a positive charge. The Journal of Physical Chemistry Letters. 2011; 2: 2300–2303. DOI: 10.1021/jz200887k

29. Neidel C, et al. Probing time-dependent molecular dipoles on the attosecond time scale. Physical Review Letters. 2013; 111 033001 [PubMed: 23909314]

30. Ott C, et al. Reconstruction and control of a time-dependent two-electron wave packet. Nature. 2014; 516: 374–378. DOI: 10.1038/nature14026 [PubMed: 25519135]

31. Kowalewski M, Bennett K, Dorfman KE, Mukamel S. Catching conical intersections in the act: Monitoring transient electronic coherences by attosecond stimulated x-ray raman signals. Phys Rev Lett. 2015; 115 193003 doi: 10.1103/PhysRevLett.115.193003 [PubMed: 26588377]

32. Keefer D, Schnappinger T, de Vivie-Riedle R, Mukamel S. Visualizing conical intersection passages via vibronic coherence maps generated by stimulated ultrafast x-ray raman signals. Proceedings of the National Academy of Sciences. 2020; 117: 24069–24075.

33. Huppert M, Jordan I, Wörner HJ. Attosecond beamline with actively stabilized and spatially separated beam paths. Review of Scientific Instruments. 2015; 86 123106 doi: 10.1063/1.4937623 [PubMed: 26724005]

34. Tachikawa H. A full dimensional ab initio direct trajectory study on the ionization dynamics of sih 4. Physical Chemistry Chemical Physics. 2002; 4: 1135–1140.

35. Püttner R, Domke M, Lentz D, Kaindl G. Si 2 p photoabsorption in sih 4 and sid 4: Molecular distortion in core-excited silane. Physical Review A. 1997; 56 1228

36. Golubev NV, Vaníek J, Kuleff AI. Core-valence attosecond transient absorption spectroscopy of polyatomic molecules. Phys Rev Lett. 2021; 127 123001 doi: 10.1103/PhysRevLett.127.123001 [PubMed: 34597071]

37. Meyer H-D, Manthe U, Cederbaum LS. The multi-configurational time-dependent hartree approach. Chemical Physics Letters. 1990; 165: 73–78.

38. Meyer, H-D, Gatti, F, Worth, GA. Multidimensional quantum dynamics: MCTDH theory and applications. John Wiley & Sons; 2009.

39. Köppel H, Domcke W, Cederbaum LS. Multimode molecular dynamics beyond the born-oppenheimer approximation. Advances in Chemical Physics. 1984; 57: 59–246.

40. Pabst S, Lein M, Wörner HJ. Preparing attosecond coherences by strong-field ionization. Phys Rev A. 2016; 93 023412 doi: 10.1103/PhysRevA.93.023412

41. Pabst S, Greenman L, Ho PJ, Mazziotti DA, Santra R. Decoherence in attosecond photoionization. Phys Rev Lett. 2011; 106 053003 doi: 10.1103/PhysRevLett.106.053003 [PubMed: 21405393]

42. Arnold C, et al. Molecular electronic decoherence following attosecond photoionisation. Journal of Physics B: Atomic, Molecular and Optical Physics. 2020; 53 164006

43. Golubev NV, Begušić T, Vaníček J. On-the-fly ab initio semiclassical evaluation of electronic coherences in polyatomic molecules reveals a simple mechanism of decoherence. Phys Rev Lett. 2020; 125 083001 doi: 10.1103/PhysRevLett.125.083001 [PubMed: 32909765]

44. Fiete GA, Heller EJ. Semiclassical theory of coherence and decoherence. Physical Review A. 2003; 68 022112 doi: 10.1103/PhysRevA.68.022112

45. Yuan G, et al. The role of transition dipole phase in atomic attosecond transient absorption from the multi-level model. Structural Dynamics. 2019; 6 054102 doi: 10.1063/1.5124441 [PubMed: 31649962]

46. Kobayashi Y, Neumark DM, Leone SR. Theoretical analysis of the role of complex transition dipole phase in XUV transient-absorption probing of charge migration. Optics Express. 2022; 30: 5673–5682. [PubMed: 35209524]

47. Kling MF, von den Hoff P, Znakovskaya I, de Vivie-Riedle R. (sub-)femtosecond control of molecular reactions via tailoring the electric field of light. Phys Chem Chem Phys. 2013; 15: 9448–9467. DOI: 10.1039/C3CP50591J [PubMed: 23695586]

48. Golubev NV, Kuleff AI. Control of charge migration in molecules by ultrashort laser pulses. Phys Rev A. 2015; 91 051401 doi: 10.1103/PhysRevA.91.051401

49. Cooper G, Burton GR, Chan Wing Fat, Brion C. Absolute oscillator strengths for the photoabsorption of silane in the valence and si 2p and 2s regions (7.5–350 ev). Chemical Physics. 1995; 196: 293–306.

50. Jarque EC, et al. Universal route to optimal few-to single-cycle pulse generation in hollow-core fiber compressors. Scientific reports. 2018; 8: 1–10. [PubMed: 29311619]

51. Harada T, Takahashi K, Sakuma H, Osyczka A. Optimum design of a grazing-incidence flat-field spectrograph with a spherical varied-line-space grating. Applied optics. 1999; 38: 2743–2748. [PubMed: 18319848]
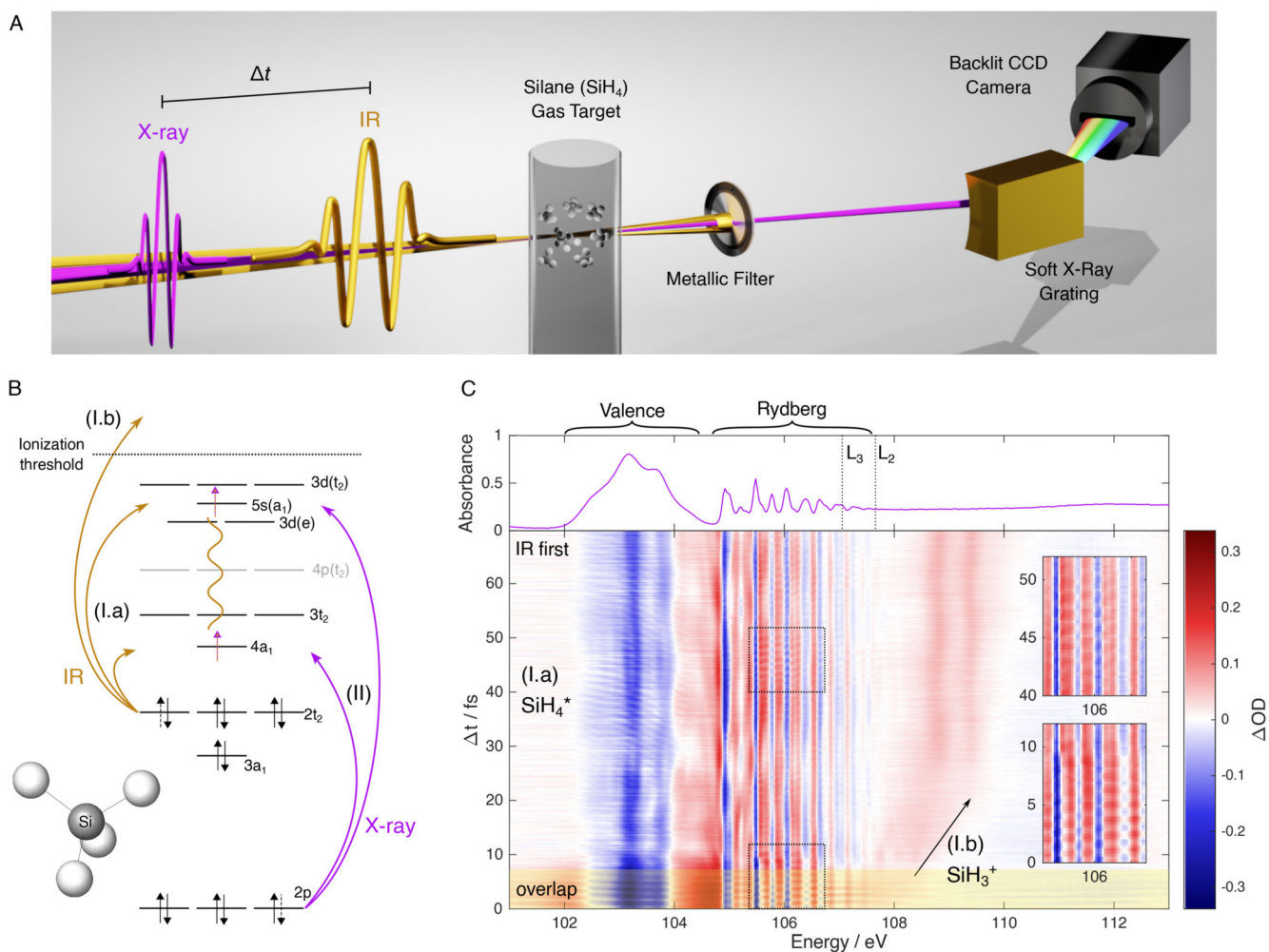
Fig. 1. Overview of experimental setup, pump-probe scheme, and data.
A) Schematic representation of the experiment. B) Molecular-orbital diagram of silane showing the ground-state configuration (black arrows), the preparation of an electronic superposition state by the pump pulse (yellow arrows), which creates electronic coherence (yellow wave), and its probing by a delayed core-level transient absorption (purple arrows). C) ATAS spectra as a function of time delay between the pump and probe pulses. The insets show a magnified view of the dotted boxes, highlighting the decay and revival of charge migration. The top panel shows the $L_{2,3}$-edge absorption spectrum of unexcited SiH_4.
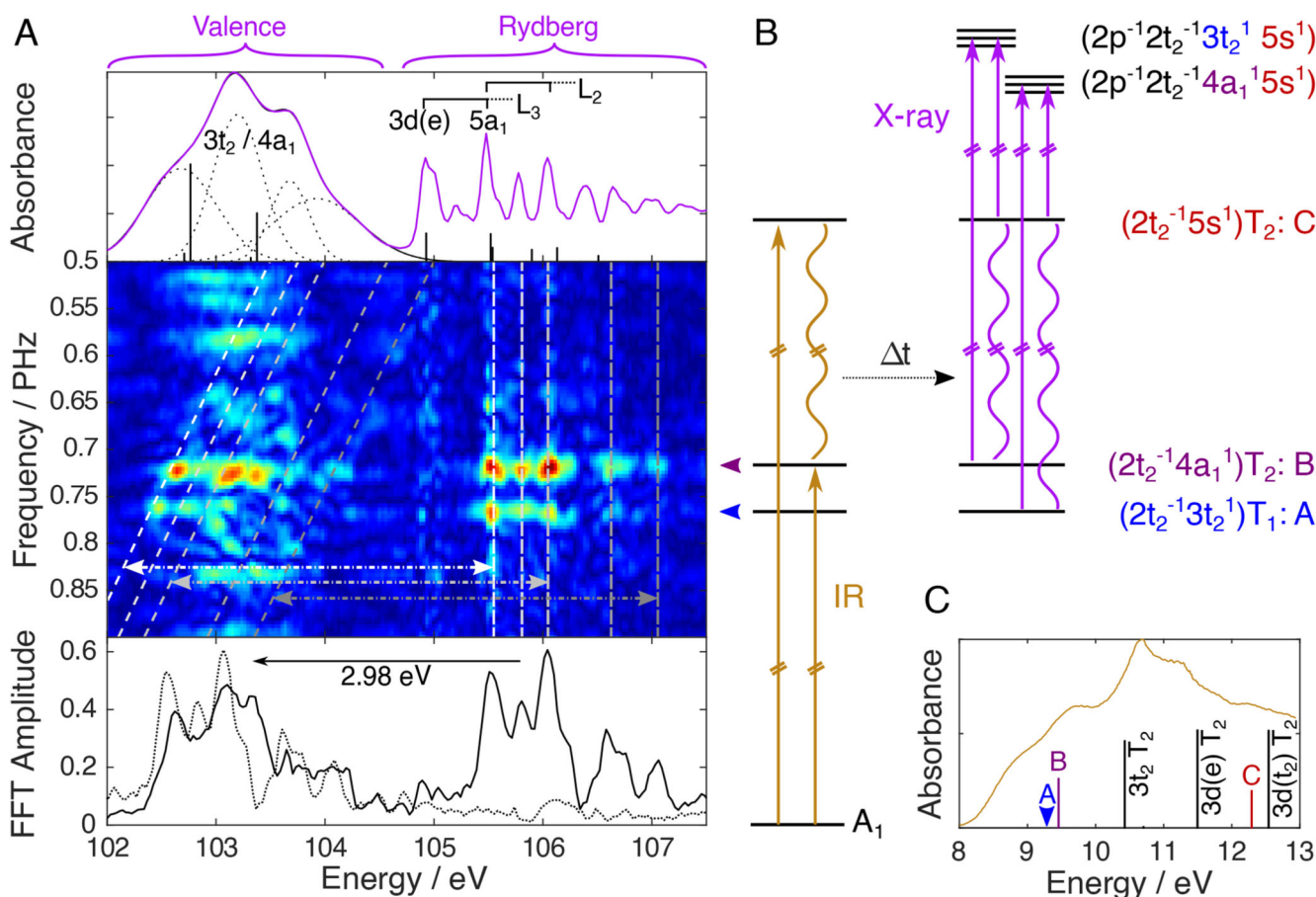
Fig. 2. Identifying the electronic states involved in charge migration.
A) Static absorption spectrum of silane at the Si $L_{2,3}$-edge with CVS-ADC(2)-x/aug-cc-pVTZ calculations (stick spectra shifted by -1.5 and -0.9 eV to account for the spin-orbit splitting of the $L_{2,3}$ edges)(top), spectrally-resolved FFT amplitude of the ATAS data (Fig. 1C) for delays above 10 fs (middle), line-out of the FFT amplitude at 0.72 PHz (bottom). B) Electronic-state diagram illustrating the preparation, time evolution, and probing of the electronic coherences (represented by waves). C) Valence absorption spectrum of silane (from (49)) and calculated electronic absorption spectrum (sticks, EOM-CCSD/aug-cc-pVTZ).
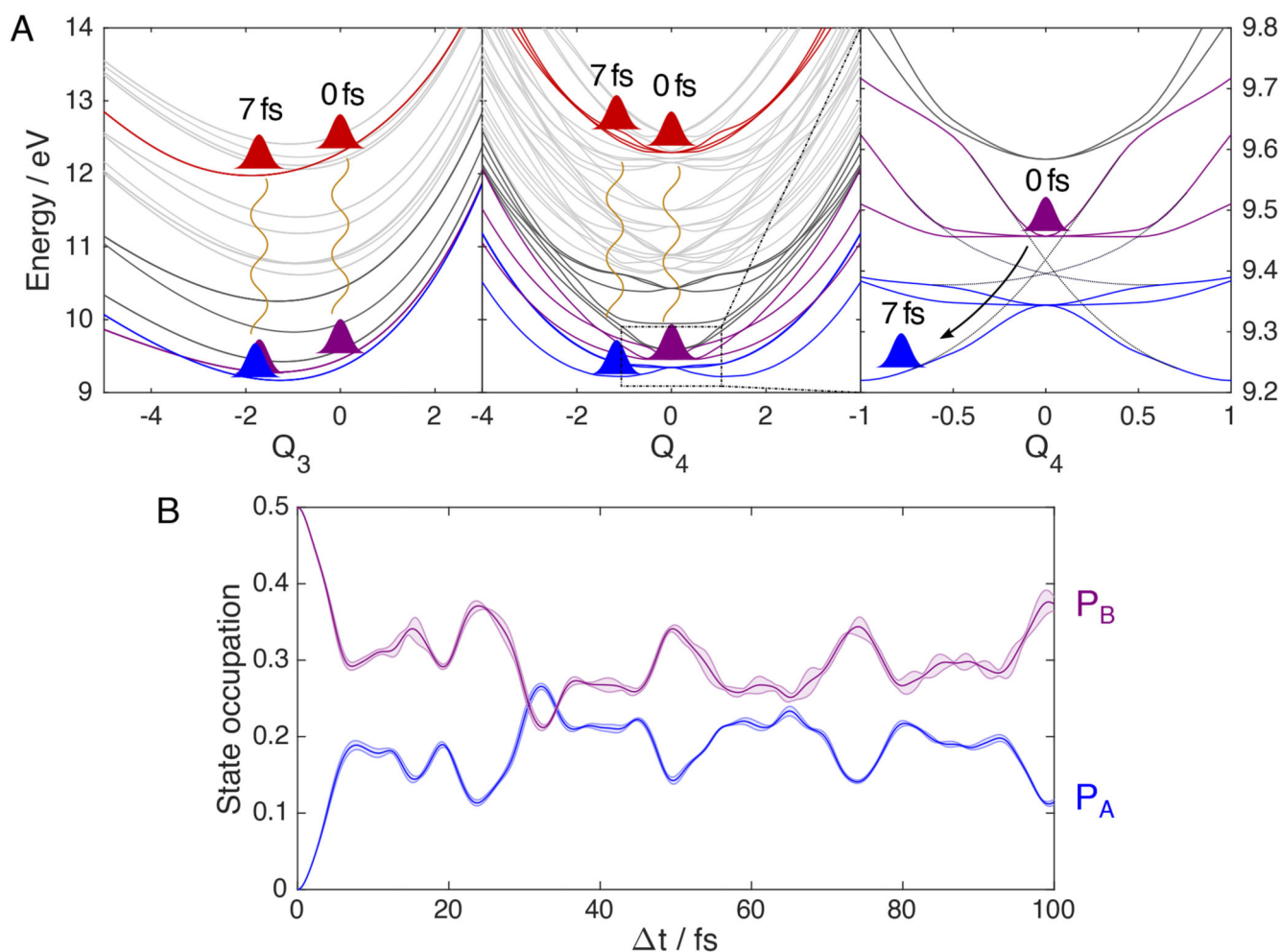
Fig. 3. Non-adiabatic transfer of electronic coherence
A) Adiabatic PES as a function of the symmetric (ν_3) and anti-symmetric (ν_4) stretching modes (left and middle). The curves have been colour-coded to reflect the electronic character of the corresponding states (see Fig. 2B for assignment). Dark-grey curves represent other states included in the MCTDH model while light-grey curves represent states excluded from the model. Magnified portion of the central panel with overlaid schematic diabatization (dotted lines) reflecting the conical intersection between the A and B states responsible for the population transfer (right). B) Diabatic MCTDH populations of the A and B states as a function of time after initialization.
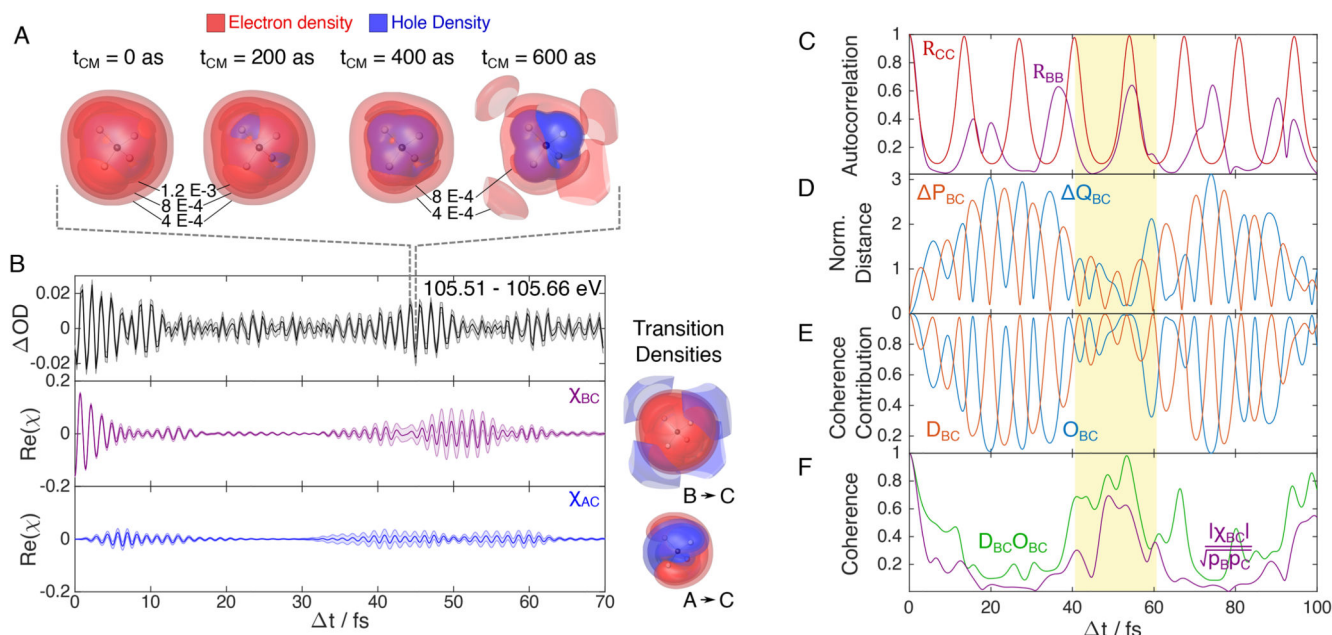
Fig. 4. Attosecond electron wavepacket, decoherence and revival.
A) Electrondensity difference between excited and unexcited molecules ($\rho_{ES}(t) - \rho_{GS}$) at selected delays covering half a quantum-beat period (as indicated by the dotted lines), isosurface values are labeled, B) Measured Fourier-filtered (0.5-1.5 PHz) OD (black, left scale) and MCTDH-calculated electronic coherences (purple/blue, right scale), the transition densities related to each coherence are shown on the right-hand side, C-F) Analysis of the decoherence and revival showing (C) the normalised MCTDH auto-correlation functions of the nuclear wavepackets in the C-Rydberg (red) and B-valence (violet) states, (D) the difference between the position and momentum expectation values of the wavepackets in the B and C states, (E) their contributions to the mutual electronic coherence, and (F) the normalised electronic coherence obtained from the semi-classical analysis (green) and from the full MCTDH calculation (violet). The revival has been highlighted in yellow for clarity. It is worth noting that the predicted revival around 100 fs might be influenced by the neglected slow vibrational modes,which become more important with increasing propagation time.
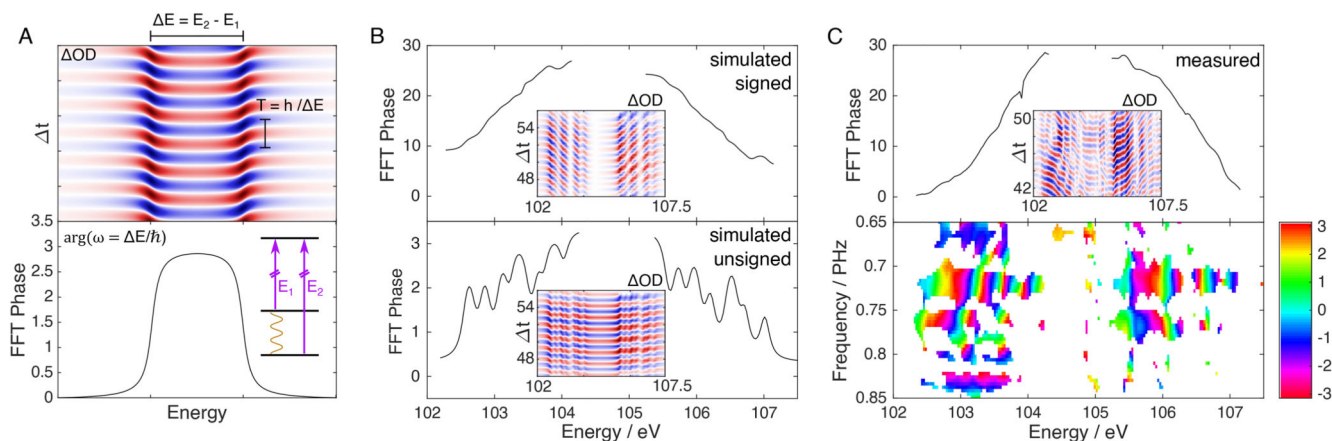
Fig. 5. Encoding of the sign of transition-dipole moments in molecular ATAS
A) The spectral signature of a quantum beat in ATAS. B) Results of the ATAS simulations
based on the MCTDH results. The top panel is obtained by selecting the relative signs of
the transition dipoles to best match the experiment (Table S4), whereas the bottom figure is
the result of choosing all transition dipoles positive. Simulated and measured ATAS results
at the time of the revival are presented alongside the corresponding phase line-outs. C)
Phase of the quantum beat extracted from the experimental transient spectrum. The bottom
panel displays the phase of the FFT shown in Fig. 2A. Areas corresponding to negligible
amplitudes have been left blank. An unwrapped line-out of this phase, taken at 0.72 PHz, is
shown in the top panel with the experimental   OD, Fourier filtered to isolate components
between 0.6 and 0.9 PHz, shown as inset.